The relation between coronal holes and coronal mass ejections during the rise, maximum, and declining phases of Solar Cycle 23

A. A. Mohamed,[1,2,3,4] N. Gopalswamy,[2] S. Yashiro,[2,3] S. Akiyama,[2,3] P. Mäkelä,[2,3] H. Xie,[2,3] and H. Jung[2,3]

[1]   We study the interaction between coronal holes (CHs) and coronal mass ejections (CMEs) using a resultant force exerted by all the coronal holes present on the disk and is defined as the coronal hole influence parameter (CHIP). The CHIP magnitude for each CH depends on the CH area, the distance between the CH centroid and the eruption region, and the average magnetic field within the CH at the photospheric level. The CHIP direction for each CH points from the CH centroid to the eruption region. We focus on Solar Cycle 23 CMEs originating from the disk center of the Sun (central meridian distance ≤15°) and resulting in magnetic clouds (MCs) and non-MCs in the solar wind. The CHIP is found to be the smallest during the rise phase for MCs and non-MCs. The maximum phase has the largest CHIP value (2.9 G) for non-MCs. The CHIP is the largest (5.8 G) for driverless (DL) shocks, which are shocks at 1 AU with no discernible MC or non-MC. These results suggest that the behavior of non-MCs is similar to that of the DL shocks and different from that of MCs. In other words, the CHs may deflect the CMEs away from the Sun-Earth line and force them to behave like limb CMEs with DL shocks. This finding supports the idea that all CMEs may be flux ropes if viewed from an appropriate vantage point.

1.   Introduction

[2]   Coronal mass ejections (CMEs) are known to interact with large-scale structures such as streamers, coronal holes, and other CMEs [see, e.g., *Gopalswamy et al.*, 2004]. These interactions lead to several observable effects such as enhanced radio emission, particle acceleration, and CME deflection. CME deflection by nearby CHs is particularly interesting because of the unexpected geospace consequences. CMEs deflected away from the Sun-Earth line may not reach Earth and hence may not cause geomagnetic storms [*Gopalswamy et al.*, 2009b]. CMEs may also be deflected toward the Sun-Earth line resulting in unusually large geomagnetic storms [*Gopalswamy et al.*, 2005].

[3]   CMEs colliding with each other can result in large changes in the trajectory of one of the CMEs [*Gopalswamy*

[1]School of Physics, University of Sydney, Sydney, New South Wales, Australia.
[2]NASA Goddard Space Flight Center, Greenbelt, Maryland, USA.
[3]Department of Physics, Catholic University of America, Washington, DC, USA.
[4]National Research Institute of Astronomy and Geophysics, Cairo, Egypt.

et al., 2001]. *Van der Holst et al.* [2002] showed using numerical simulation that a fast expanding CME collided with a northern-hemisphere helmet streamer, leading to a deflection and a wavelike deformation propagating outward along the streamer. *Gopalswamy et al.* [2009a] reported on the EUV wave reflection from a CH and they were able to measure the kinematics of the reflected waves and confirmed the wave nature of the EUV disturbances.

[4]   The field lines from the polar CHs are suggested to guide high-latitude CMEs toward the equator [*Gopalswamy et al.*, 2000, 2003; *Gopalswamy and Thompson*, 2000; *Plunkett et al.*, 2001; *Filippov et al.*, 2001; *Cremades et al.*, 2006; *Gopalswamy et al.*, 2009b]. It is also suggested that CMEs trajectories are influenced by the initial magnetic polarity of a flux rope relative to the background magnetic field [*Byrne et al.*, 2010]. They showed that CMEs, in earlier phase of their evolution, are deflected from a high-latitude source region into a non-radial trajectories indicated by a change in their inclination angles, expanding on previous work. Other theoretical work by *Chané et al.* [2005], using a simulation of the CMEs superposed on different steady state solar wind models, demonstrated that the initial magnetic field polarity inside a flux rope is essential for the evolution of CMEs.

[5]   *Gopalswamy et al.* [2009b] found that several "driverless" (DL) shocks observed in situ at L1 were

Table 1. The Measured Parameters of the Different CHs for the 15 October 1998 Event[a]

	CH Centroid	Area, A (km^2)	Average Magnetic Field, $\langle B \rangle$ (G)	Distance, d (km)	**f** (G)	fPA (deg)
CH1	N54E27	9.6×10^{10}	5.4	4.6×10^5	2.5	211°
CH2	N12E08	1.2×10^{10}	−1.9	1.6×10^5	0.9	312°
CH3	N00E10	1.4×10^{10}	−1.7	2.9×10^5	0.3	337°
CH4	S62E02	3.4×10^{10}	−4.4	9.3×10^5	0.2	358°
CH5	N49W21	5.9×10^9	3.1	3.8×10^5	0.1	153°

[a]F = 2.3 G, FPA = 238°.

associated with CMEs launched near the disk-center. These shocks were called driverless because there was no inter-planetary CMEs (ICMEs) observed behind the shocks. It is normal to observe DL shocks due to limb CMEs, but not disk-center CMEs. The CMEs driving the DL shocks were deflected away from the Sun-Earth line by CHs, and the corresponding ICMEs did not hit Earth [*Gopalswamy et al.*, 2009b]. Their study found that all the DL shocks originating near the solar disk center occurred during the declining phase of Solar Cycle 23. They defined and computed a coronal hole influence parameter (CHIP) to quantify the CME-CH interaction. They found that the CHIP had higher values for the DL shocks than the shocks with drivers. In another study, *Gopalswamy et al.* [2010a] investigated the effect of the CHs on two sets of CMEs originating close

to the disk center: one resulting in magnetic clouds (MCs) driving shocks and the other resulting in DL shocks. They estimated an angular deflection to be 20°−60° for the DL shocks.

[6] Most CMEs that arrive at Earth originate close to the disk center of the Sun (within the longitude range of ±30°) [see, e.g., *Bravo and Blanco-Cano*, 1998; *Gopalswamy et al.*, 2000; *Cane and Richardson*, 2003]. From geometrical considerations, the MCs are associated with disk-center CMEs heading toward Earth, while the non-disk-center CMEs become non-MCs (or ejecta), and finally the shocks without discernible ejecta are observed as DL shocks are due to their associated CMEs are ejected almost orthogonal to the Sun-Earth line. This suggests that the CMEs ejected at intermediate angles may appear as non-MCs to an observer near the Sun- Earth line and that the viewing angle may probably the reason for ICMEs without an observable flux rope structure [*Marubashi*, 1996; *Gopalswamy*, 2006; *Riley et al.*, 2006; *Owens et al.*, 2005].

[7] The disk-center non-MCs seem to deviate from this expected behavior. One possibility is that the non-MC CMEs may be subject to slightly larger CH influence than the MCs. Such an effect has important implications for the flux rope nature of ICMEs. If the CHIP for non-MC CMEs is found to be larger than that for MC CMEs, one could conclude that non-MC CMEs do not show a flux rope structure purely for geometrical reasons: the central axis of the CME-flux rope system will be missed by a single-spacecraft

Table 2. Disk-Center MC Events During the Three Phases of Solar Cycle 23

	Shock		MCs		CME						CHIP	
Phase	Date	Time (UT)	Start Time (UT)	Duration (h)	Date	Time (UT)	Source Location	V (km/s)	MPA	FPA	$\Delta\psi$	F (G)
Rise	1997/01/10	0052	10/0500	22	01/06	1510	S18E06	136	180°	25°	155°	0.8
	1997/05/15	0115	15/1200	14.5	05/12	0530	N21W08	464	264°	352°	88°	0.2
	1997/09/21	0410	21/0900	16	09/17	2028	N45W16	377	263°	200°	63°	4.6
	1998/10/18	1928	19/0400	26.5	10/15	1004	N22W01	262	264°	307°	43°	1.1
Maximum	1999/04/16	1110	16/2018	23	04/13	0330	N16E00	291	194°	301°	107°	1.9
	1999/08/08	1744	09/0500	23.25	08/03	0550	N23W04	222	355°	230°	25°	0.3
	2000/02/20	2100	21/2000	25.5	02/17	2130	S29E07	728	184°	336°	152°	0.3
	2000/07/15	1418	15/2000	16	07/14	1054	N22W07	1674	273°	201°	72°	5.4
	2000/07/28	0639	29/0100	13	07/25	0330	N06W08	528	168°	291°	123°	8.2
	2000/08/11	1851	12/0606	19	08/09	1630	N20E12	702	12°	159°	147°	1.0
	2000/09/17	1700	18/0154	21.5	09/16	0518	N14W07	1215	3°	323°	40°	5.3
	2000/10/12	2236	13/1600	23	10/09	2350	N01W14	798	318°	195°	123°	1.1
	2000/11/06	0920	06/1750	19	11/03	1826	N02W02	291	57°	178°	121°	0.8
	2001/03/19	1130	19/1830	43	03/16	0350	N11W09	271	312°	348°	36°	1.4
	2001/04/11	1619	11/2200	10	04/10	0530	S23W09	2411	166°	337°	171°	5.0
	2001/04/28	0502	28/1500	9	04/26	1230	N20W05	1006	37°	62°	25°	0.5
	2002/03/18	1313	20/0200	16.5	03/15	2306	S08W03	957	309°	240°	69°	0.9
	2002/04/17	1101	18/0100	25	04/15	0350	S15W01	720	198°	335°	137°	1.1
	2002/05/18	1951	19/0354	10	05/16	0050	S23E15	600	158°	360°	158°	1.3
Declining	2002/08/01	0510	01/0900	10.5	07/29	1207	S10W10	526	301°	203°	98°	4.4
	2002/08/01	2305	02/0600	13.5	07/29	2330	N12W16	360	354°	223°	131°	5.2
	2003/08/17[a]	1340	18/0430	24	08/14	2006	S10E02	378	25°	93°	68°	1.3
	2003/10/29[b]	0600	29/1100	16	10/28	1130	S20E02	2495	H15°	160°	145°	1.1
	2003/10/30[b]	1620	31/0200	10	10/29	2054	S19W09	2029	H190°	255°	65°	4.6
	2004/07/24[a]	0532	24/1530	20.5	07/22	0830	N04E10	899	210°	193°	17°	1.6
	2004/11/07	1759	07/2230	13.5	11/04	0206	N09E05	1111	21°	94°	73°	2.5
	2005/05/15	0219	15/0915	14.75	05/13	1712	S12E11	1689	H2°	42°	40°	0.7
	2005/05/20[a]	0334	20/0718	22	05/17	0326	S15W00	449	54°	334°	80°	2.0
	2005/06/12[a]	0659	12/1500	20	06/09	1436	N09E16	125	52°	202°	150°	0.3

[a]MCs were not included in the work by *Gopalswamy et al.* [2009b].
[b]MCs re-analyzed due to slight revision in their solar source locations. The prefix H in column 7 denotes the halo CMEs with unidentified central position angle (CPA).

Shock: 15/ 02:19 MC Start time:15/ 09:15 MC End time 16/ 00:00
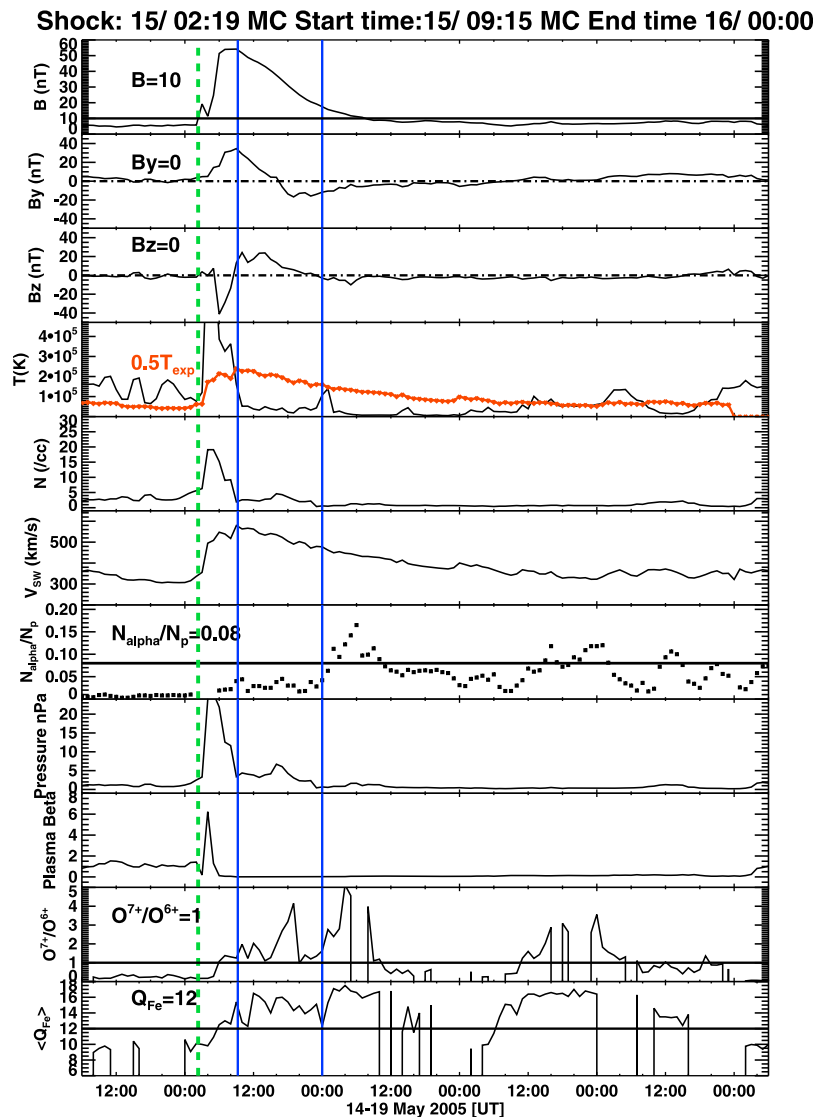
Figure 1. Example of an ICME observed by ACE (a classic MC) following the IP shock (dashed vertical line) on 15 May 2005. The event shows enhanced, smoothly rotating magnetic field (B_z). The start and end time of the ICME interval are marked by vertical solid lines. Other ICME characteristics are visible e.g., proton temperature depression below $0.5T_{exp}$ line is shown as the red horizontal line; declining solar wind speed profile; enhanced $N\alpha/Np$ (>0.08), decrease in flow pressure, proton density similar to pre event, plasma beta and finally the enhancement in oxygen and iron charge states.

observation due to the CH deflection [*Gopalswamy et al.*, 2009a, 2009b].

[8] In the present paper, we extend previous studies to the rise and maximum phases of Solar Cycle 23, considering all the ICMEs that originate close to the disk center. In particular, we investigate how the CHIP for non-MCs compares with that of MCs and DL shocks.

[9] In section 2 we present the selection criteria for the events and the method of data analysis. We also explain the method for identifying ICMEs and CHs, and present the solar source distributions of CMEs associated with MCs and DL shocks. We define the CHIP and discuss the coronal environment of CMEs resulting in MCs and non-MCs in section 3. We compare the average CHIP and average alignment angles for MCs and non-MCs during the

three phases of the solar cycle in section 4. In section 5 we summarize the results and present our conclusions.

2. Data Selection and Method of Analysis

[10] The starting point of this investigation is a set of shock-driving ICMEs listed in work by *Gopalswamy et al.* [2010b, Table 1]. The list includes shocks driven by either MCs and non-MCs and DL shocks during May 1996 to December 2006. For each ICME, there is a corresponding CME observed by the Large Angle and Spectrometric Coronagraph (LASCO) [*Brueckner et al.*, 1995] on board the Solar and Heliospheric Observatory (SOHO) mission. From this list we extract only those ICMEs whose solar sources are close to the disk-center, i.e., Central Meridian Distance (CMD) is within 15°.
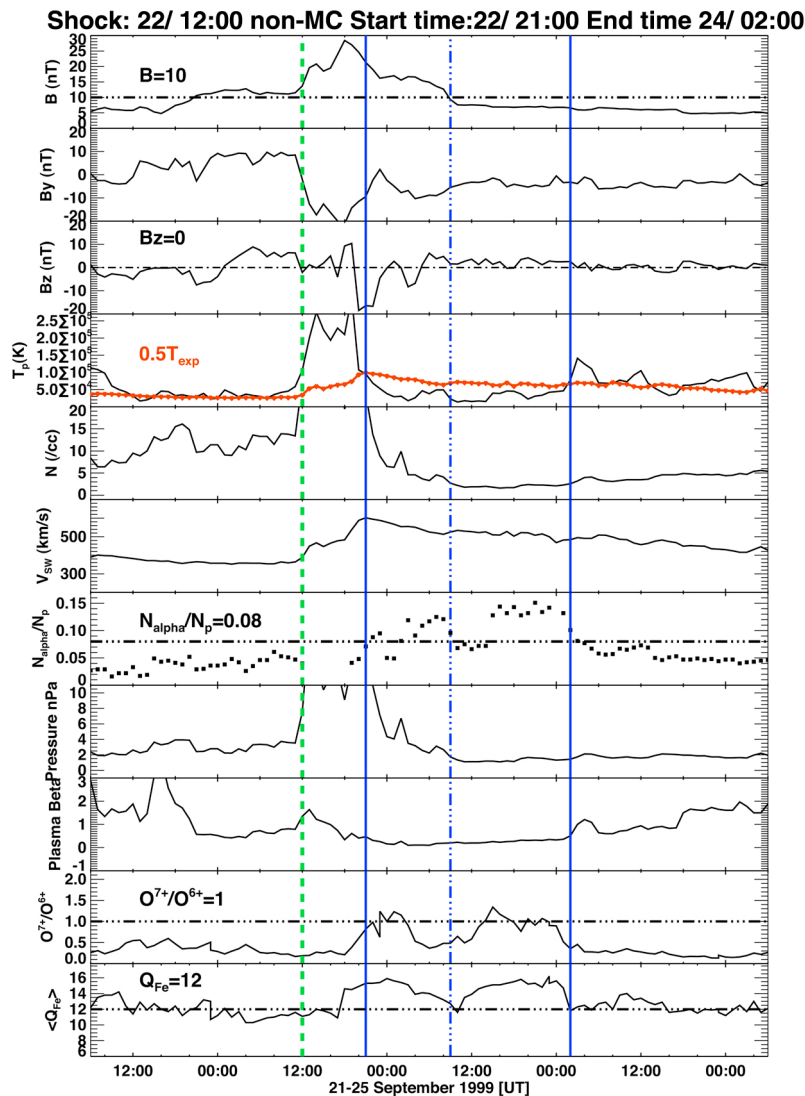
Figure 2. Example of a non-MC observed by ACE following an IP shock (dashed green vertical line) on 22 September 1999. This event shows more irregular and weaker magnetic field than the MC in Figure 1. The start and end time of ICME interval are marked by vertical solid lines. Other ICME signatures are visible e.g., proton temperature depression below $0.5T_{exp}$ line is shown as the red horizontal line; declining solar wind speed profile; enhanced $N\alpha/Np$ (>0.08), decrease in flow pressure, proton density, plasma beta and the enhancement in oxygen and iron charge states. The dash-dotted line at 9:00 UT shows the division of the non-MC interval into two regions each satisfies the ICME signatures.

[11] The extracted ICMEs are listed in Tables 1 (MCs) and 2 (non-MCs). We use the list of ICMEs in the declining phase [*Gopalswamy et al.*, 2009b, Table 3] and divide them into MCs and non-MCs. We added another 4 MC events (denoted by "*a*") that were not included in their list. Two MCs (denoted by "*b*") and 2 non-MCs (denoted by "*c*") were reanalyzed due to slight revision in their solar source locations. We also use the set of DL shocks from *Gopalswamy et al.* [2009b], which correspond to ICMEs severely affected by coronal hole deflection.

2.1. ICME Identification for Selected Events

[12] *Gopalswamy et al.* [2009b] identified the MCs and ejecta behind interplanetary (IP) shocks from the following

data: Advanced Composition Explorer (ACE) [*Stone et al.*, 1998] data in GSE coordinates for the magnetic field magnitude (B) and its Y and Z components (B_y, B_z), solar wind bulk flow speed (V), proton temperature (T_p), proton density (N_p), the alpha to proton density ratio N_α/N_p, flow pressure (n_{pa}), plasma beta, and oxygen and iron charge states. The expected solar wind proton temperature ($0.5\ T_{exp}$) based on relations by *Lopez and Freeman* [1986] and *Neugebauer et al.* [2003] was used as a primary criterion. $N_\alpha/N_p > 0.08$ was used as a secondary criterion and it should be met during the T_p depression for at least part of the interval.

[13] In the present work, we followed the same procedure to identify the end of the ejecta so that we can define
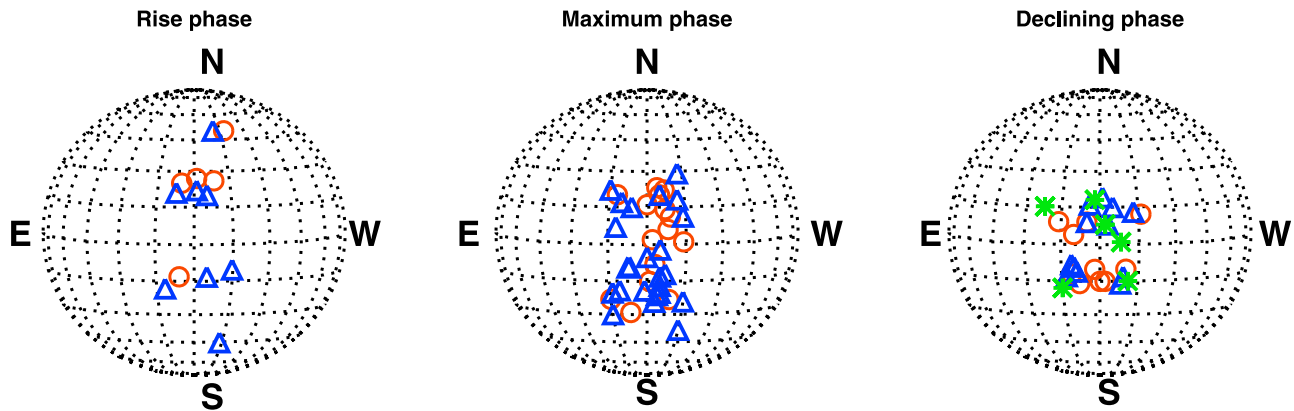
Figure 3. Solar sources of CMEs that resulted in MCs (red circles) and non-MCs (blue triangles) for the rise, maximum and declining phases of the solar cycle 23. The sources of the DL shocks are represented by green stars.

the ICME interval. Figures 1 and 2 show two examples of shock-driving ICMEs: an MC on 2005 May 15 at 02:19 UT and a non-MC on 1999 September 22 at 12:00 UT. The MC event occurred during the declining phase and the non-MC occurred during the maximum phase. It is clear that the T_p is enhanced in the sheath region between the shock and the start of ejecta (this region is common to all shocks irrespective of whether the ICME signatures exist or not). The sheath lasts for ∼7 h in the 2005 May 15 event and ∼9 h in the 1999 September 22 event. The enhancement in the magnetic field (B) and the depression of T_p below 0.5 T_{exp} mark the onset of the ICME (09:15 UT and 21:00 for 2005 May 15 and 1999 September 22, respectively). N_α/N_p was definitely enhanced above 0.08 with respect to the pre-shock values in the case of the non-MC event, while for the MC event the enhancement was below 0.08 for the entire interval. The enhancement in N_α/N_p was below 0.08 but is shown above 0.08 for what may be considered a second event following the first one. Note also the continuation of the T_p depression and most of the other signatures beyond the described MC interval which may correspond to a single or several non-MCs following up the first MC. The duration of the MC event is 14.75 h and ∼29 h for the non-MC event. The end times of the MC and non-MC are determined to be at 00:00 UT and 02:00 UT on 16 May 2005 and 24 September 1999, respectively. For the 15 May 2005 MC event, the onset time is ∼3 hours later than the time reported by *Richardson and Cane* [2010] and also in the MC list based on the observations of the Magnetic Field Investigation (MFI) [*Lepping et al.*, 1995] on-board Wind: (http://wind.gsfc.nasa.gov/mfi/mag_cloud_pub1.html). We are using the T_p depression as the primary criterion in defining the ICME boundaries. Our end time is only 2 hours later than their reports. Interestingly, most of the signatures persist until about 2:00 UT on 22 May 2005 suggesting another non-MC or ejecta following this MC event. In general there are slight discrepancies in the identification of ICME boundaries among various authors but the differences are only about a few hours.

[14] In the 22 September 1999 non-MC event, the ICME interval seems to be divided into two regions both satisfying the ICME signatures at ∼9 UT on 23 September 1999

marked by the vertical dash-dotted line shown in Figure 2. This suggests that there is more than one non-MC following each others resulting from the eruption of successive CMEs.

[15] Figure 1 shows that the 2005 May 15 MC event is unipolar, i.e. the B_z component is fully north (FN) and the direction of the Y-component rotates smoothly from east to west. So the internal magnetic cloud structure can be classified as ENW (see *Bothmer and Schwenn* [1994], *Mulligan et al.* [1998], and *Gopalswamy* [2008] for details on the different MC types). The examples in Figures 1 and 2 show how a typical sequence proceeds at 1 AU: the shock followed by the sheath ($T_p > 0.5T_{exp}$), and ejecta ($T_p < 0.5T_{exp}$). Similar identification of the boundaries was done for the 72 ICMEs studied in this paper.

2.2. Solar Source Locations of the ICMEs

[16] The association between ICMEs and the corresponding CMEs observed by SOHO/LASCO was made by examining all CMEs that occurred over a window of 0.5 to 5 days prior to the shock arrival time at 1 AU [*Gopalswamy et al.*, 2009b]. The solar source locations of the CMEs are defined as the heliographic coordinates of the associated eruption such as H-alpha flare and soft X-ray flare (Solar Geophysical Data) or the location of the associated disk activity, e.g., post eruption arcades or EUV dimming (see *Gopalswamy et al.* [2007, 2009b] for details on CME source identification). Here we take the source identification provided by *Gopalswamy et al.* [2010b].

[17] Figure 3 shows the solar source locations of CMEs associated with MCs (circles), non-MCs (triangles) and the DL shocks (stars). The sources are at the highest latitudes in the rise phase, at intermediate latitudes in the maximum phase and at the lowest latitudes in the declining phase because the emergence of active regions follow the well-known butterfly diagram. The number of MCs and non-MCs among the disk-center events is the largest during solar maximum and the least during the rise phase. This is directly related to the increased solar activity during solar maximum. The solar source locations of the five disk-center CMEs associated with DL shocks have been discussed in detail by *Gopalswamy et al.* [2009b].
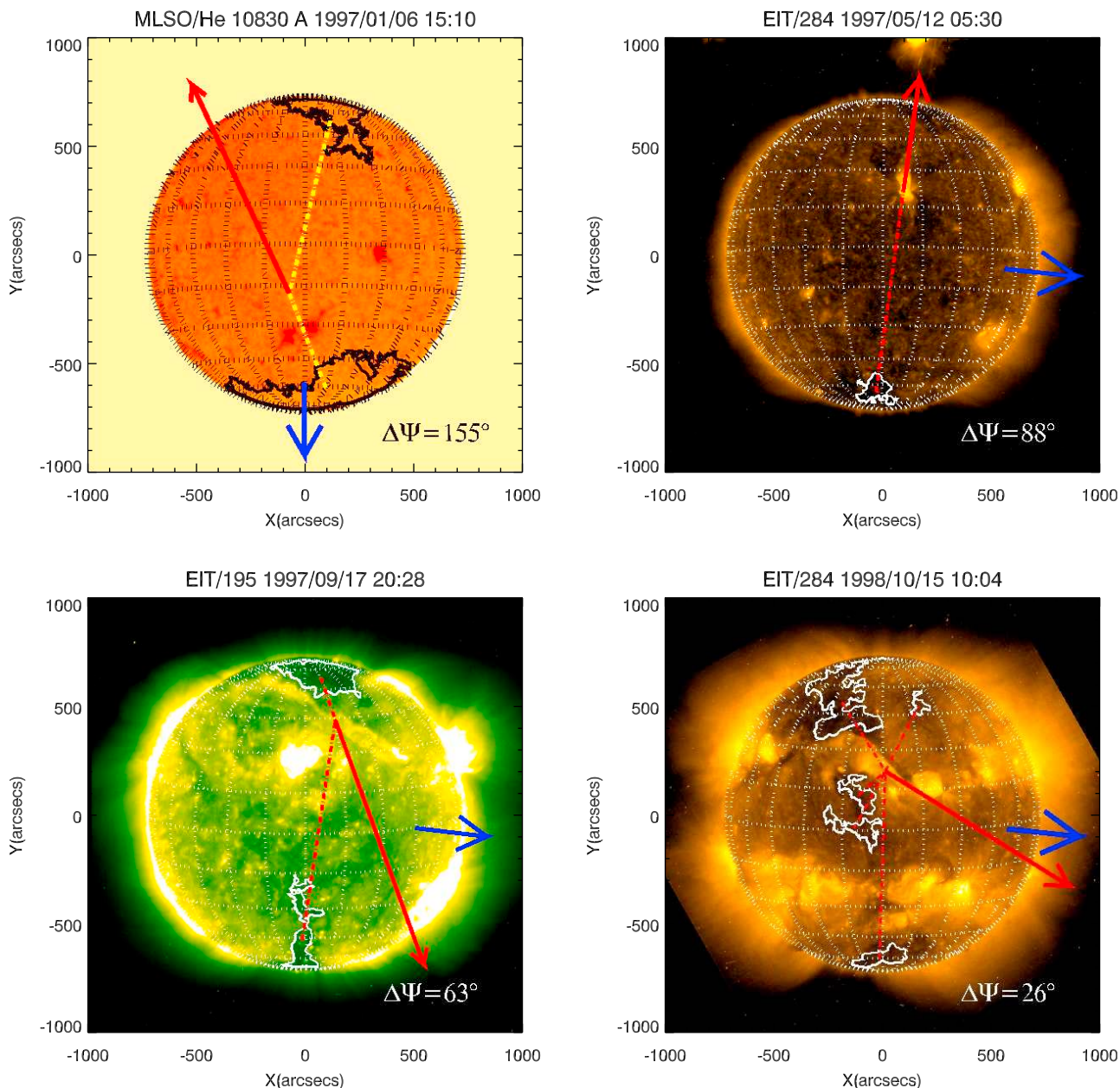
Figure 4. Coronal holes and eruption centers of CMEs on 6 January 1997, 12 May 1997, 17 September 1997, and 15 October 1998. The heliographic grid spacing is 15°. For the first event, the CH contour out lines 75 % of the median brightness of the solar disk when in the He 10830 Å image, while for the other events in the 284 Å image the contours are at 50 % of the median EUV intensity of the solar disk. The dashed red lines connect the eruption region to the centroid of each coronal hole. The red arrow points from the solar source of the CME to the direction of the CHIP. The blue arrow indicates the measurement position angle (MPA) along which the CME height time history has been measured. The alignment angle which is the difference ($\Delta\psi$) between FPA and MPA, is noted on each image.

2.3. Coronal Hole Identification

[18] We use 284 Å images from the Extreme ultraviolet Images Telescope (EIT) [*Delaboudinieére et al.*, 1995] on-board SOHO, to identify the coronal holes. The areas that are dim in EUV are the CHs, where the magnetic field is predominantly unipolar. EIT 284 Å images are preferred compared to X-ray images because, X-ray images are not available for all the events. EIT 284 Å images are preferred over EIT 195 Å images because the coronal holes are clearer in these images compared to those at 195 Å. However, 195 Å images occasionally used whenever there was lack of data at 284 Å. The CHs are defined as areas outlined by a single contour at the 50% level of the median EUV intensity of the solar disk (see Figure 4). In order to obtain photospheric magnetic fields within the CHs, we use the line of sight magnetograms obtained by the Michelson Doppler Imager (MDI) [*Scherrer et al.*, 1995] onboard SOHO. We have also used He 10830 Å images from the

1997/05/12 05:30 UT

B_{Mean}=-5.3 G

CH Centroid=S66E06

CH Corrected area [A]=2.8x10^{10} km^2
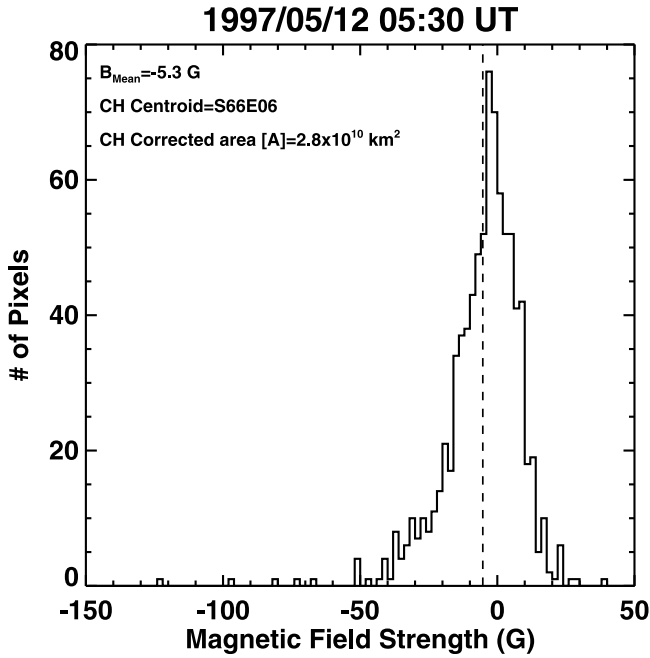
Figure 5. Number of pixels for the southern CH during the 12 May 1997 event are plotted versus the magnetic field strength. The average magnetic field strength is denoted by the dashed line. The CH centroid and area are shown on the graph.

Mauna Loa Solar Observatory for some events such as the 6 January 1997 MC due to data gaps in other wavelengths as shown in Figure 4. The coronal holes appear as bright regions in He 10830 Å images so that the contour outlining the coronal hole encloses an area (~75%) in which the brightness exceeds the median brightness of the solar disk at this wavelength.

[19] In the magnetograms obtained by SOHO/MDI, the areas within the CHs that have a minor opposite magnetic polarity are eliminated. We also eliminated the areas of nearby filaments that appear dark in the EIT images as well.

[20] The average magnetic field in the coronal hole is determined from the SOHO/MDI magnetograms obtained in the synoptic mode (one magnetogram every 96 min). The CH contour from the EIT 284 Å images is superposed on the magnetogram after rotating the magnetogram to the time of the EIT image.

[21] Figure 5 shows the distribution of magnetic field strengths in the CH of 12 May 1997 event at the CME eruption time (5:30 UT). The magnetic field distribution is near-Gaussian and slightly asymmetric.

3. The Coronal Hole Influence Parameter (CHIP)

[22] The CHIP has a magnitude (F) that depends on the CH area, the distance between the CH and the eruption region, and the magnetic field within the CH at the photospheric level. The direction of F acts along a position angle (FPA), which is the direction along which the resultant of all the coronal holes acts. Thus, for each CH, we have

$$\mathbf{f} = \left[\langle B \rangle A / d^2 \right] \mathbf{e_f} \qquad (1)$$

where $\mathbf{f}$ is a vector and $\mathbf{e_f}$ is the unit vector, which acts in the direction from the CH centroid to the eruption region. The dimension of (1) is in gauss (G). Then, we calculate the vector sum of the influence parameters over all coronal holes present on the disk to obtain the CHIP magnitude, F, and the direction of $\mathbf{F}$ (position angle FPA).

$$\mathbf{F} = \sum \mathbf{f}_i, \qquad i = 1, \ldots, N, \qquad (2)$$

where N is the total number of coronal holes present on the disk. The magnetic field lines inside the CH are assumed to be radial and therefore a correction to the projection effects for the field strength and the CH area is applied using the known angle of the CH centroid with respect to the line of sight:

$$A = \acute{A} \cos \phi \qquad (3)$$

$$B = \acute{B} \cos \phi, \qquad (4)$$

where A and B are the corrected area and magnetic field inside the CH, respectively. $\acute{A}$ and $\acute{B}$ are the observed CH area and magnetic field inside the CH, respectively, and ϕ is the angle between the CH centroid and the line of sight.

3.1. CHIP for MCs and Non-MCs

[23] Figure 4 illustrates the coronal environment of the four CMEs during the rise phase (6 January 1997, 12 May 1997, 17 September 1997, and 15 October 1998) that resulted in MCs observed on 10 January 1997 at 00:52 UT, 15 May 1997 at 01:15 UT, 21 September 1997 at 16:51 UT, and 18 October 1998 at 19:28 UT, respectively. For the first event, we use the He 10830 Å image from the Mauna Loa Solar Observatory and for others we use the EIT 284 Å images. There were no magnetograms obtained by SOHO/MDI for the 15 October 1998 event so, we used the MDI data of 21 October 1998 and rotated the image to the CME time on 15 October 1998.

[24] For the 15 October 1998 event, the largest CH is located in the northeast (NE) and has its centroid at N54E27. The CH centroid is at a distance (d) of ~4.6 × 10^5 km from the eruption site (N22W01). The CH area (A) corrected for the projection effects is ~9.6 × 10^{10} km^2. The average magnetic field ($\langle B \rangle$) obtained from the MDI magnetogram ~5.4 G. Applying the formula in equation (1), we obtain f_1 = 2.5 G and the position angle in which f_1 is directed is 211°. The second CH is also located in the northeast quadrant and has its centroid at N12E08. Using $A_2 = 1.2 \times 10^{10}$ km^2 and $d_2 = 1.6 \times 10^5$ km, and $\langle B_2 \rangle = -1.9$ G, we obtain $f_2 \sim 0.9$ G directed along a position angle of 312°. The third CH is located close to the disk center with its centroid at N00E10. For this CH, $A_3 = 1.4 \times 10^{10}$ km^2, $d_3 = 2.9 \times 10^5$ km, and $\langle B_3 \rangle = -1.7$ G, so $f_3 \sim 0.3$ G directed along a position angle of ~337°. The fourth CH is located in the south with its centroid is at S62E02. From $A_4 = 3.4 \times 10^{10}$ km^2, $d_4 = 9.3 \times 10^5$ km, and $\langle B_4 \rangle = -4.4$ G, we get f_4 as ~0.2 G with a position angle ~358°. The last CH is located in the northwest (NW) quadrant at N49W21 with $d_5 = 3.8 \times 10^5$ km, $A_5 = 5.9 \times 10^9$ km^2, $\langle B_5 \rangle \sim 3.1$ G, so $f_5 \sim 0.1$ G with a position angle ~153°. The net influence of the five CHs is $F = 2.3$ G pointed along the PA of 238°. We denote this

Table 3. Disk-Center Non-MC Events During the Three Phases of Solar Cycle 23

	Shock		Non-MCs		CME						CHIP	
Phase	Date	Time (UT)	Start Time (UT)	Duration (h)	Date	Time (UT)	Source Location	V (km/s)	MPA	FPA	$\Delta\psi$	F (G)
Rise	1997/10/24	1115	24/1700	1.5	10/21	1803	N16E07	523	90°	169°	79°	1.8
	1997/12/10	0430	10/1840	16.25	12/06	1027	N45W10	397	296°	315°	19°	0.5
	1998/04/07	1655	08/0100	7.25	04/04	0246	S23E12	237	22°	16°	6°	1.3
	1998/05/03	1700	03/1900	6	05/01	1510	S18W05	585	126°	189°	63°	0.2
	1998/05/04	0200	04/1000	19	05/02	1406	S15W15	938	331°	298°	33°	0.2
	1998/06/25	1610	26/0200	17	06/22	0734	S50W15	278	199°	192°	7°	0.2
	1998/11/07	0800	07/2200	6	11/04	0754	N17W01	377	349°	324°	25°	0.1
	1998/11/13	0140	13/0430	2.5	11/09	1818	N15W05	325	338°	320°	18°	0.5
Maximum	1999/06/26	1925	27/2200	4	06/24	1331	N29W13	975	335°	332°	3°	0.8
	1999/07/02	0023	02/0600	3	06/29	1954	S14E01	397	320°	359°	39°	2.4
	1999/08/04	0146	04/0254	3.5	08/01	2150	N27E16	347	9°	1°	8°	0.4
	1999/09/15	2000	16/0300	19	09/13	1731	N15E06	444	62°	359°	63°	9.9
	1999/09/22	1200	22/2100	29	09/20	0606	S20W05	604	14°	48°	34°	37
	1999/10/21	0213	21/1800	8.5	10/18	0006	S30E15	144	184°	58°	126°	9.8
	1999/10/28	1210	29/0300	12.25	10/25	1426	S38W15	511	172°	1°	171°	0.9
	2000/01/22	0023	22/1750	8	01/18	1754	S19E11	739	45°	29°	16°	2.5
	2000/07/10	0600	11/0200	10.5	07/07	1026	N17E10	453	193°	18°	175°	1.0
	2000/07/11	1122	11/2248	28.25	07/08	2350	N18W12	483	339°	279°	60°	1.7
	2000/07/26	1858	27/0500	14	07/23	0530	S13W05	631	166°	268°	102°	1.4
	2000/08/10	0510	10/1900	18	08/06	2306	S24W15	597	233°	332°	99°	2.9
	2000/10/05	0323	05/1313	3.25	10/02	0350	S09E07	525	107°	61°	46°	10.0
	2000/11/26	0530	27/0800	20	11/24	0530	N20W05	1289	313°	340°	27°	1.0
	2001/02/20	0230	20/1300	2.5	02/15	1354	N07E12	625	17°	349°	28°	2.3
	2001/03/03	1130	04/0400	8	02/28	1450	S17W05	313	263°	342°	79°	1.9
	2001/03/22	1400	22/2330	7	03/19	0526	S20W00	389	184°	300°	116°	0.7
	2001/04/11	1412	11/2230	4.5	04/09	1554	S21W04	1192	211°	336°	125°	2.6
	2001/08/12	1110	12/1416	5.75	08/09	1030	N11W14	479	255°	270°	15°	1.2
	2001/10/11	1650	12/0416	4.25	10/09	1130	S28E08	937	184°	316°	132°	1.5
	2002/05/11	1030	11/1300	9	05/08	1350	S12W07	614	229°	323°	94°	2.3
	2002/05/20	0340	20/1113	23.75	05/17	0127	S20E14	461	145°	50°	95°	1.6
	2002/05/30	0215	30/0709	10	05/27	1327	N22E15	1106	35°	165°	130°	4.6
Declining	2002/07/17	1550	18/1200	21	07/15	2130	N19W01	1300	45°	355°	50°	4.4
	2002/11/09	1759	10/0730	7.5	11/06	0606	S13E13	485	162°	191°	29°	1.4
	2004/01/22[c]	0110	22/0800	22	01/20	0006	S16W05	965	H224°	87°	137°	1.8
	2004/12/11	1303	12/2256	20	12/08	2026	N08W03	611	H301°	233°	77°	1.2
	2005/01/16	0927	16/1400	16	01/15	0630	N16E04	2049	H359°	113°	114°	0.6
	2005/01/17	0715	17/1600	6.5	01/15	2306	S15W05	2861	H323°	178°	145°	1.8
	2005/02/17	2159	18/1500	15	02/13	1106	S11E09	584	129°	218°	89°	5.8
	2005/05/29	0915	30/0200	21	05/26	2126	S08E11	420	61°	114°	53°	1.8
	2005/07/10	0256	10/1106	41	07/07	1706	N09E03	683	H39°	154°	115°	1.7
	2005/09/02	1332	02/1830	4.5	08/31	1130	N13W13	825	H287°	191°	96°	3.4
	2005/09/15	0825	15/1424	3.5	09/13	2000	S09E10	1866	H149°	100°	49°	1.3
	2006/08/19[a]	1051	20/0000	10	08/16	1630	S16W08	888	H161°	182°	21°	0.4

[a]Non-MCs re-analyzed due to slight revision in their solar source locations. The prefix H in column 7 denotes the halo CMEs with unidentified Central Position Angle (CPA). halo CMEs.

position angle as FPA. Note that this FPA is close to the FPA of the first CH because it has the maximum CHIP (2.5). The red arrow in Figure 4 represents the direction along FPA = 238°. Height-time measurements of CMEs are made along a position angle at which the CME appears to be moving the fastest, and is referred to as the measurement position angle (MPA). If MPA and FPA are close to each other, we think that the CH influence is significant. If they are too far apart, the coronal hole influence may be insignificant. For the 1998 October 15 CME MPA = 264°, so the difference between FPA and MPA is 26°. The previous measured parameters of the CHs are displayed in Table 1.

[25] Tables 2 and 3 list the MCs and non-MCs during the three phases of Solar Cycle 23, respectively, and summarize various parameters of the associated eruptions and CHs: the date and time of IP shocks in yyyy/mm/dd hhmm format (first and second columns); the ICME start time in dd/hhmm

format (third column); the ICME duration in hours (fourth column); the corresponding white-light CME (date and time of the first appearance of the CME in mm/dd hhmm format in the fifth and sixth columns); the heliographic coordinates of the eruption region (seventh column); the average sky-plane speed of the CME obtained from LASCO observations (eighth column); the measurement position angle (MPA in degrees) of the CME (ninth column); the PA (tenth column); and the alignment angle ($\Delta\psi$) in degrees and (F) in gauss (eleventh and twelfth columns, respectively).

[26] During the three phases of the solar cycle, Tables 1 and 2 show that the CHIP (F) values range from 0.2 to its largest value of 8.2 G for MCs while a moderate values are existed around 5 G. In the case of non-MCs, the F values vary from extremely lower 0.1 G to another extremely higher value of 37 G in the case of 20 September, 1999 (see Table 3). Few other large values $F \sim 10$ G existed in the maximum phase.
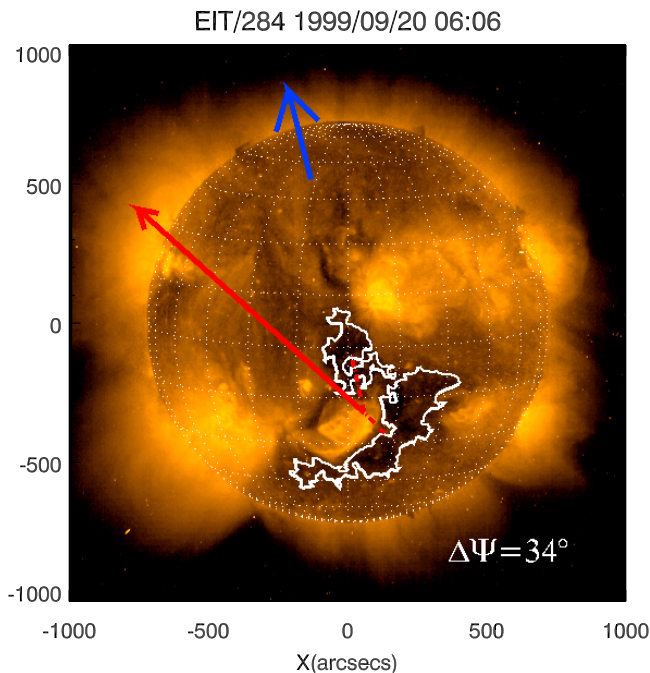
Figure 6. EIT image of the 20 September 1999 non-MC event. The eruption is from S27 but the CME propagates northward. This is certainly due to the influence of the CH to the south and west of the eruption region. The alignment angle is also very small, confirming the influence of the CH.

3.2. The Peculiar Case of 20 September 1999 Non-MC Event That Occurred at the Maximum Phase

[27] The 20 September 1999 event has a CHIP value = 37 G, which is very high compared to those of the other events in this study. This is due to the very large area ($A = 9.03 \times 10^{10}$ km^2) of the CH (centroid at S27W12), which is close ($d = 1.15 \times 10^5$ km) to the eruption region (S20W05) and has also a relatively strong magnetic field $\langle B \rangle = 5.6$ G as shown in Figure 6. The very high CHIP value and FPA angle = 48° make it possible that the CME was deflected toward the Sun-Earth line as an example of the opposite case of the driverless shocks, where the CMEs of the DL shocks were deflected away from the Sun-Earth line so that they did not hit Earth as discussed by *Gopalswamy et al.* [2009b]. It is worth noting that the resultant FPA = 48° and the alignment angle of 34° is consistent with the significant deflection. Without such deflection, this CME would not have reached Earth. This event indicates also that the distance between the CH centroid and the source location is the most

effective parameter in determining the CHIP than the CH area and CH average magnetic field.

4. The Average Coronal Hole Influence Parameter

[28] The average CHIP values (F^{av} and $\Delta\psi^{av}$) are presented in Table 4. Both values are determined for the rise, maximum and declining phases denoted by subscripts r, m, and d, respectively. $F_r^{av} = 1.7$ G for MCs is higher (almost three times) than that of the non-MCs ($F_r^{av} = 0.6$ G). In the maximum phase, $F_m^{av} = 2.4$ G for MCs is comparable to non-MCs ($F_m^{av} = 2.9$ G). For the combined set of MCs and non-MCs, $F_m^{av} = 2.7$ G. In these calculations, we have excluded the 20 September 1999 non-MC, which has very high F. If we include this event ($F = 37$ G), we obtain $F_m^{av} = 4.6$ G for non-MCs. In the declining phase, we obtain $F_d^{av} = 2.1$ G for non-MCs. For the combined MCs and non-MCs, we obtain $F_d^{av} = 2.3$ G. This value for the combined set of MCs and non-MCs in the declining phase is consistent with that reported by *Goplaswamy et al.* [2009b] to be $F_d^{av} = 2.55$ G. The F values computed for MCs and non-MCs are significantly lower than the value for DL shocks ($F = 5.8$ G).

[29] Table 4 shows that the average alignment angle for non-MCs is less than that for MCs during the three phases. The average alignment angles for non-MCs is intermediate between the DL shocks (lowest) and MCs (highest). Since a smaller alignment angle implies a greater coronal hole influence, we can see that the non-MCs are affected more by

Table 4. The Average CHIP and Alignment Angle for MCs, Non-MCs, and DL Shocks

Class	Average CHIP			Alignment Angle		
	F_r^{av} (G)	F_m^{av} (G)	F_d^{av} (G)	$\Delta\psi_r^{av}$	$\Delta\psi_m^{av}$	$\Delta\psi_d^{av}$
MCs	1.7	2.4	2.4	86°	98°	97°
Non-MCs	0.6	2.9	2.1	44°	60°	77°
MCs+non-MCs	1.2	2.7	2.3	65°	79°	87°
DL shocks	-	-	5.8	-	-	40°
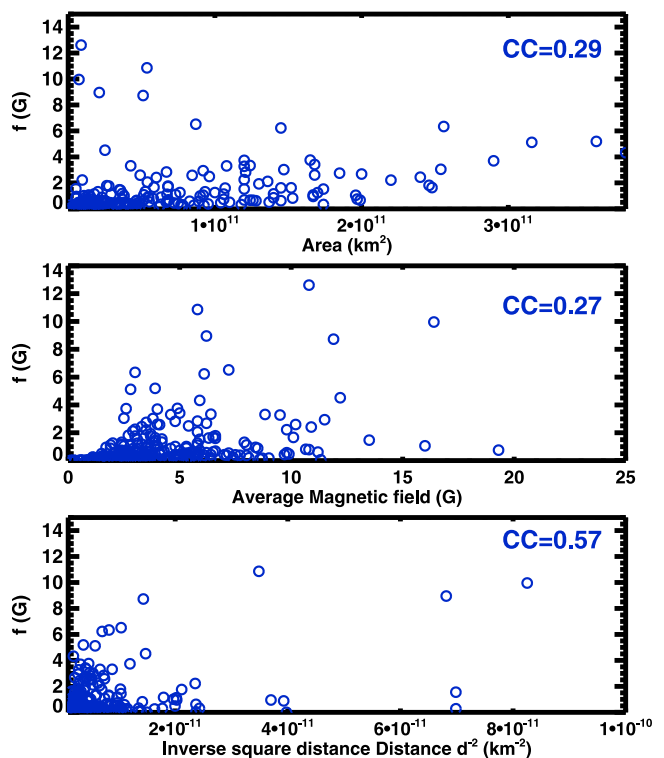
Figure 7. The individual CHIP (f) versus the CH parameters: area (A), average magnetic field ($\langle B \rangle$), and inverse square distance (d^{-2}) for 308 CHs on the solar disk in the 72 events during the three phases of the solar cycle 23. The correlation coefficient is the highest for f vs d^{-2}.

the coronal holes, consistent with the discussion based on F values. Also, the lowest value is obtained for the non-MCs in the rise phase, $\Delta\psi_r^{av} = 44°$, which is very close to that for DL shocks ($\Delta\psi_d^{av} = 40°$) given by *Gopalswamy et al.* [2009b].

[30] Recalling that the highest average CHIP value is obtained for non-MCs at maximum phase $F_m^{av} = 2.9$ (about half of that for DL shocks), we may say that the non-MCs resemble the DL shocks in that both have large F value and small alignment angle. This finding suggests that non-MCs may have a flux rope structure similar to the MCs but the CME deflection by CHs make them appear as non-flux ropes.

[31] Figure 7 shows the dependence of f on the CH area (A), average magnetic field strength ($\langle B \rangle$), and the distance between the CH centroid and eruption region (d^{-2}). The highest correlation coefficient refers to (d^{-2}) (CC = 0.57), while it is smaller for A (CC = 0.29) and $\langle B \rangle$ (CC = 0.27). We computed the confidence level for our correlation coefficients using a simple code based on the Fisher transformation ($z(CC) = 1/2\ln[(1 + CC)/(1 - CC)]$) *Fisher* [1921]. The resulted confidence level for the correlation coefficient of (d^{-2}), A, and $\langle B \rangle$ is: 100%, 100%, and 99.9%, respectively. This indicates that distance is the most important quantity in equation 1. One reason for the high percentage of the confidence level is due to the large sample size (n = 308) used.

5. Discussion and Conclusions

[32] The main result of this study is that the influence of CHs on CMEs that erupt close to the disk center is found to be the strongest for DL shocks, intermediate for non-MCs and the smallest for MCs during the three phases of Solar Cycle 23. This result gives further support to the suggestion by *Gopalswamy et al.* [2009b] that the trajectories of the CMEs are highly affected when the eruptions occur from source regions close to CHs, which act as if they were magnetic barriers guiding the CME propagation. This result indicates that the difference in observed structure between MCs and non-MCs may be due to the difference in the relative position of the ICME magnetic flux rope structure to the observer at 1 AU. The results support the hypothesis that non-MCs are due to CMEs that are ejected at intermediate angles relative to the Sun-Earth line. The higher CHIP and lower alignment angles in the case of CMEs associated with non-MCs are consistent with this hypothesis. The statistics presented in this paper can be improved by investigating the CHs influence on the CMEs that erupt from an intermediate distance from the solar disk center (i.e., central meridian distance ≤30°).

[33] Our results confirm that the propagation of CMEs can be severely affected by the presence of coronal holes nearby. We also see a clear ordering of the interplanetary events by the CHIP. Driverless shocks are affected the most, non-MCs intermediate and MCs the least. When there is no influence from the coronal holes, all CMEs from the disk center are likely to appear as MCs at Earth. Of course, one has to consider additional factors such as inherent non-radial eruptions that might mimic deflection. Observations of the flux rope structure near the Sun is difficult for Earth-directed CMEs due to the occulting disk that blocks their central part;

flux-rope structure is readily observed in a subset of the limb CMEs [see, e.g., *Chen et al.*, 1997]. The observations from the post-eruption arcades in EUV, H-alpha ribbons, and soft X-rays do not show any difference between the eruptions that end up as MCs and non-MCs. One of the important evidences that supports the flux rope scenario is the relation between the azimuthal fluxes of MCs measured in the solar wind and the reconnected magnetic flux measured in the flare ribbons on the solar surface [*Qiu et al.*, 2007]. By examining the flare geometry for MCs and non-MCs, it may be possible to infer how CME propagation may affect the final appearance of CMEs at 1 AU as MCs or non-MCs.

[34] Future theoretical models and observations rely on the STEREO mission to provide additional information to address the geometrical aspects of CMEs and ICMEs. We would like to point out that the physical mechanism of CME deflection at the boundaries between open and close regions of the solar atmosphere and in the Heliosphere is yet to be worked out.

[35] The main results of this study may be summarized as follows:

[36] 1. The average value of the CHIP is the lowest for the non-MCs and MCs in the rise phase, $F_r^{av} = 1.7$ G and 0.6 G, respectively.

[37] 2. For MCs, the average CHIP has the smallest value in the rising phase $F_r^{av} = 1.7$ G, where as the CHIP values are comparable for maximum and declining phases ($F = 2.4$).

[38] 3. The CHIP increases from the rise through the maximum to the declining phase.

[39] 4. The CHIP ($F_m^{av} = 2.9$ G) for non-MCs during the maximum phase is fairly large when compared to the rise and declining phases. One usually expects to have MCs associated with disk-center CMEs, the large number of non-MCs from the disk center may indicate that deflection by coronal holes makes MCs appear as non-MCs at Earth.

[40] 5. The highest CHIP ($F = 5.8$ G) is obtained for the DL shocks. The average CHIP (F) for MCs and non-MCs is two times lower than that for the DL shocks obtained by *Gopalswamy et al.* [2009b].

References

Bothmer, V., and R. Schwenn (1994), Eruptive prominences as sources of magnetic clouds in the solar wind, *Space Sci. Rev.*, *70*(1–2), 215–220.

Bravo, S., and X. Blanco-Cano (1998), Signatures of interplanetary transients behind shocks and their associated near-surface solar activity, *Ann. Geophys.*, *16*, 359–369.

Brueckner, G. E., et al. (1995), The large angle spectroscopic coronagraph (LASCO), *Sol. Phys.*, *162*, 357–402.

Byrne, J. P., S. A. Maloney, R. T. James McAteer, J. M. Refojo, and P. T. Gallagher (2010), Propagation of an Earth-directed coronal mass ejection in three dimensions, *Nat. Commun.*, *1*(6), 74, doi:10.1038/ncomms1077.

Cane, H. V., and I. Richardson (2003), Interplanetary coronal mass ejections in the near-Earth solar wind during 1996–2002, *J. Geophys. Res.*, *108*(A4), 1156, doi:10.1029/2002JA009817.

Chané, E., C. Jacobs, B. van der Holst, S. Poedts, and D. Kimpe (2005), On the effect of the initial magnetic polarity and of the background wind on the evolution of CME shocks, *Astron. Astrophys.*, *432*(1), 331–339.

Chen, J., R. A. Howard, G. E. Brueckner, R. Santoro, J. Krall, S. E. Paswaters, O. C. St. Cyr, R. Schwenn, P. Lamy, and G. M. Simnett (1997),

Evidence of an erupting magnetic flux rope: LASCO coronal mass ejection of 1997 April 13, *Astrophys. J.*, *490*, L191.

Cremades, H., V. Bothmer, and D. Tripathi (2006), Properties of structured coronal mass ejections in Solar Cycle 23, *Adv. Space Res.*, *38*, 461–465, doi:10.1016/j.asr.2005.01.095.

Delaboudinieére, J.-P., et al. (1995), EIT: Extreme-Ultraviolet Imaging Telescope for the SOHO mission, *Sol. Phys.*, *162*, 291–312.

Filippov, B. P., N. Gopalswamy, and A. V. Lozhechkin (2001), Non-radial motion of eruptive filaments, *Sol. Phys.*, *203*, 119–130, doi:10.1023/A:1012754329767.

Fisher, R. A. (1921), On the "probable error" of a coefficient of correlation deduced from a small sample, *Metron*, *1*, 3–32.

Gopalswamy, N. (2006), Properties of interplanetary coronal mass ejections, *Space Sci. Rev.*, *124*(1–4), 145–168.

Gopalswamy, N. (2008), Solar connections of geoeffective magnetic structures, *J. Atmos. Sol. Terr. Phys.*, *70*, 2078–2100, doi:10.1016/j.jastp.2008.06.010.

Gopalswamy, N., and B. J. Thompson (2000), Early life of coronal mass ejections, *J. Atmos. Sol. Terr. Phys.*, *62*(16), 1457–1469.

Gopalswamy, N., A. Lara, R. P. Lepping, M. L. Kaiser, D. Berdichevsky, and O. C. St. Cyr (2000), Interplanetary acceleration of coronal mass ejections, *Geophys. Res. Lett.*, *27*, 145–148, doi:10.1029/1999GL003639.

Gopalswamy, N., A. Lara, M. L. Kaiser, and J.-L. Bougeret (2001), Near-Sun and near-Earth manifestations of solar eruptions, *J. Geophys. Res.*, *106*, 25,261–25,277, doi:10.1029/2000JA004025.

Gopalswamy, N., S. Yashiro, A. Lara, M. L. Kaiser, B. J. Thompson, P. T. Gallagher, and R. A. Howard (2003), Large solar energetic particle events of Cycle 23: A global view, *Geophys. Res. Lett.*, *30*(12), 8015, doi:10.1029/2002GL016435.

Gopalswamy, N., S. Yashiro, S. Krucker, G. Stenborg, and R. A. Howard (2004), Intensity variation of large solar energetic particle events associated with coronal mass ejections, *J. Geophys. Res.*, *109*, A12105, doi:10.1029/2004JA010602.

Gopalswamy, N., S. Yashiro, G. Michalek, H. Xie, R. P. Lepping, and R. A. Howard (2005), Solar source of the largest geomagnetic storm of Cycle 23, *Geophys. Res. Lett.*, *32*, L12S09, doi:10.1029/2004GL021639.

Gopalswamy, N., S. Yashiro, and S. Akiyama (2007), Geoeffectiveness of halo coronal mass ejections, *J. Geophys. Res.*, *112*, A06112, doi:10.1029/2006JA012149.

Gopalswamy, N., S. Yashiro, M. Temmer, J. Davila, W. T. Thompson, S. Jones, R. T. J. McAteer, J. P. Wuelser, S. Freeland, and R. A. Howard (2009a), EUV wave reflection from a coronal hole, *Astrophys. J.*, *691*, L123–L127, doi:10.1088/0004-637X/691/2/L123.

Gopalswamy, N., P. Mäkelä, H. Xie, S. Akiyama, and S. Yashiro (2009b), CME interaction with coronal holes and their interplanetary consequences, *J. Geophys. Res.*, *114*, A00A22, doi:10.1029/2008JA013686.

Gopalswamy, N., P. Mäkelä, H. Xie, S. Akiyama, and S. Yashiro (2010a), Solar sources of driverless interplanetary shocks, *AIP Conf. Proc.*, *1216*, 452–458, doi:10.1063/1.3395902.

Gopalswamy, N., H. Xie, P. Mäkelä, S. Akiyama, S. Yashiro, M. L. Kaiser, R. A. Howard, and J.-L. Bougeret (2010b), Interplanetary shocks lacking type II radio bursts, *Astrophys. J.*, *710*, 1111–1126, doi:10.1088/0004-6256/710/2/1111.

Lepping, R. P., et al. (1995), The Wind magnetic field investigation, *Space Sci. Rev.*, *71*, 207–229.

Lopez, R. E., and J. W. Freeman (1986), The solar wind proton temperature velocity relationship, *J. Geophys. Res.*, *91*, 1701–1705.

Marubashi, K. (1996), Corotating and transient structures of the interplanetary magnetic fields at Venus and Earth, *AIP Conf. Proc.*, *382*, 522–525, doi:10.1063/1.51441.

Mulligan, T., C. T. Russell, and J. G. Luhmann (1998), Solar cycle evolution of the structure of magnetic clouds in the inner heliosphere, *Geophys. Res. Lett.*, *25*, 2959–2962, doi:10.1029/98GL01302.

Neugebauer, M., et al. (2003), Genesis on-board determination of the solar wind flow regime, *Space Sci. Rev.*, *105*, 661–679.

Owens, M. J., C. N. Arge, H. E. Spence, and A. Pembroke (2005), An event-based approach to validating solar wind speed predictions: High-speed enhancements in the Wang-Sheeley-Arge model, *J. Geophys. Res.*, *110*, A12105, doi:10.1029/2005JA011343.

Plunkett, S. P., B. J. Thompson, O. C. St. Cyr, and R. A. Howard (2001), Solar source regions of coronal mass ejections and their geomagnetic effects, *J. Atmos. Sol. Terr. Phys.*, *63*(5), 389–402.

Qiu, J., Q. Hu, T. Howard, and V. Yurchyshyn (2007), On the magnetic flux budget in low-corona magnetic reconnection and interplanetary coronal mass ejections, *Astrophys. J.*, *659*(1), 758–772.

Richardson, I. G., and H. V. Cane (2010), Near Earth interplanetary coronal mass ejections during Solar Cycle 23 (1996–2009): Catalog and summary of properties, *Sol. Phys*, *264*, 189–237, doi:10.1007/s11207-010-9568-6.

Riley, P., C. Schatzman, Cane, H. V., I. G. Richardson, and N. Gopalswamy (2006), On the rates of coronal mass ejections: Remote solar and in situ observations, *Astrophys. J.*, *647*(1), 648–653.

Scherrer, P. H., et al. (1995), The Solar Oscillations Investigation—Michelson Doppler Imager, *Sol. Phys.*, *162*, 129–188.

Stone, E. C., A. M. Frandsen, R. A. Mewaldt, E. R. Christian, D. Margolies, J. F. Ormes, and F. Snow (1998), The Advanced Composition Explorer, *Space Sci. Rev.*, *86*(1–4), 1–22, doi:10.1023/A:1005082526237.

Van der Holst, B., L. Van Driel-Geszteelyi, and S. Poedts (2002), CME shock coronal streamer-observation and MHD simulation, in *Proceedings of the 10th European Solar Physics Meeting*, *Eur. Space Agency Spec. Publ.*, ESA SP-506, 71–74.

S. Akiyama, H. Jung, P. Mäkelä, H. Xie, and S. Yashiro, Department of Physics, Catholic University of America, Washington, DC 20064, USA.

N. Gopalswamy, NASA Goddard Space Flight Center, Greenbelt, MD 20771, USA.

A. A. Mohamed, School of Physics, University of Sydney, Sydney, NSW 2006, Australia. (amaal.shahin@nasa.gov)